Discrete wavelet transform application in a CNN-based reverse time migration with multiple energy

Shang Huang and Daniel O. Trad

ABSTRACT

In seismic imaging, image resolution and accuracy are affected by migration approaches. Deep learning has recently been considered an alternative and efficient way to improve image quality. In this project, discrete wavelet transform (DWT) is applied with U-Net on migration data containing multiple energy. The neural network approximates the inverse of the Hessian to obtain high-quality reflectivity prediction. Results show that the DWT subband helps the model learn smooth input, extract critical features from data, and enhance image resolution. Multiple energy provides valuable information for subsurface structure expanding prediction illumination.

INTRODUCTION

Seismic imaging is a process for estimating rock parameters from seismic data (Schuster, 2020). Migration, is one way seismic imaging to detect and gain information from a subsurface structure. It generates reflectivity maps locating seismic events and collapsing energy to correct places (Gray et al., 2001). Compared with traditional depth migration methods, reverse time migration (RTM) (Baysal et al., 1983; Whitmore, 1983; McMechan, 1983; Levin, 1984) can handle lateral velocity variations, such as steep geologic structures. Least-squares reverse time migration (LSRTM) (Dong et al., 2012), as an advanced migration approach, can updates the reflectivity iteratively with improved accuracy. However, RTM and LSRTM face two problems: limited aperture due to primary reflections and poor image quality because of an insufficient source-receiver system. One alternative way to expand the illumination aperture is using multiple energy in the RTM (Liu et al., 2011; Li et al., 2017; Wang et al., 2017; Zhang et al., 2020). RTM with multiple energy (RTMM) can also help refine image accuracy and resolution.

In recent years, a helpful approach to enhance image quality is deep learning. It can learn features from the non-linear relationship between seismic data and rock parameters. Many researchers have used deep learning applications in the RTM or LSRTM (Wu et al., 2018; Kaur et al., 2020; Vamaraju et al., 2021; Torres and Sacchi, 2021, 2022; Zhang et al., 2022). These methods mitigate artifacts and foster resolution by training a machine-learning network. In other words, those networks have the stable architecture to deliver a high-quality rock parameter recovery. Mentioning about the image recovery, discrete wavelet transform combined with neural networks has been used as a tool for feature extraction (Ghazali et al., 2007), de-noising (Wang et al., 2010; Suraj et al., 2014), super-resolution in deep learning (Wu et al., 2022), and seismic data reconstruction in geophysics (Liu et al., 2022). The process of obtaining reflectivity prediction from seismic imaging results is similar to image recovery.

To mitigate the two problems we discussed above: limited aperture and poor image quality; in this project, we apply the discrete wavelet transform in a convolutional neural network-based reverse time migration with multiple energy. RTM with multiple energy can expand subsurface illumination and improve image accuracy. Discrete wavelet transform in deep learning can learn features from migrated data and enhance image resolution.

THEORY

Discrete Wavelet Transform (DWT)

A discrete wavelet transform (DWT) is a wavelet transform that decomposes a signal into a set of basic wavelet functions of different frequencies. The DWT can perform multi-resolution signal analysis, capturing both frequency and time location information (Acharya and Ray, 2005). The result decomposed by wavelet transform from a digital signal includes lower-frequency and higher-frequency subbands. Lower-frequency subbands have finer frequency resolution and coarser time resolution compared to the higher-frequency subbands.

DWT in one dimension

Based on Acharya and Ray (2005), the idea of multi-resolution analysis is to approximate a function $f(t)$ at different levels of resolution. There are two functions in the multi-resolution analysis: the mother wavelet $\psi(t)$ and the scaling function $\phi(t)$. Wavelet functions are dilated, translated and scaled versions of a common mother wavelet. The dilated and translated versions of the scaling function are given by:

$$\phi_{m,n}(t) = 2^{-m/2}\phi(2^{-m}t - n) \tag{1}$$

where m and n are integers. For fixed m, the set of scaling functions $\phi_{m,n}(t)$ are orthonormal. By the linear combinations of the scaling function and its translations, we can generate a set of functions

$$f(t) = \sum_n \alpha_n \phi_{m,n}(t) \tag{2}$$

The multi-resolution analysis decomposes a signal into two parts-one approximation of the original signal from finer to coarser resolution and the other detailed information that was lost due to the approximation.

$$f_m(t) = \sum_n a_{m+1,n}\phi_{m+1,n} + \sum_n c_{m+1,n}\psi_{m+1,n} \tag{3}$$

where $f_m(t)$ denotes the value of input function $f(t)$ at resolution 2^m, $c_{m+1,n}$ is the detail information, and $a_{m+1,n}$ is the coarser approximation of the signal at resolution 2^{m+1}. The functions $\phi_{m+1,n}$ and $\psi_{m+1,n}$, are the dilation and wavelet basis functions (orthonormal).

The decomposition of signals using the discrete wavelet transform can be expressed in terms of finite impulse response (FIR) filters. The wavelet coefficients for the signal $f(t)$ then can be decided by

$$\begin{cases} c_{m,n}(f) = \sum_k g_{2n-k} a_{m-1,k}(f) \\ a_{m,n}(f) = \sum_k h_{2n-k} a_{m-1,k}(f) \end{cases} \tag{4}$$

where g and h are the high-pass and low-pass filters, The recursive algorithm to compute DWT in different levels using equation 4 is called Mallat's Pyramid Algorithm. Since the synthesis filters h and g have been derived from the orthonormal basis functions ϕ and ψ, these filters give exact reconstruction

$$a_{m-1,i}(f) = \sum_n h_{2n-i} a_{m,n}(f) + \sum_n g_{2n-i} c_{m,n}(f) \tag{5}$$

Given the input discrete signal $x(n)$, it will be filtered parallelly by a low-pass filter (h) and a high-pass filter (g) at each transform level. The two output streams are then subsampled by simply dropping the alternate output samples in each stream to produce the low-pass subband y_L and high-pass subband y_H.

$$\begin{cases} y_L(n) = \sum_{i=0}^{\tau_L - 1} h(i)x(2n-i) \\ y_H(n) = \sum_{i=0}^{\tau_H - 1} g(i)x(2n-i) \end{cases} \tag{6}$$

where τ_L, and τ_H are the lengths of the low-pass (h) and high-pass (g) filters respectively.

DWT in two dimensions

The simple approach for 2D implementation of the DWT is to perform a standard 1D DWT row-wise to produce an intermediate result and then perform the same 1D DWT column-wise on this intermediate result to produce the final result. The two-dimensional scaling functions can be expressed as separable functions, which are the product of two one-dimensional scaling functions such as $\phi_2(x, y) = \phi_1(x)\phi_1(y)$, which is the same for the wavelet function $\psi(x, y)$ as well.

If an image has M rows and N columns, applying the one-dimensional transform in each row, two subbands are produced in each row with a size of M x $\frac{N}{2}$. Then applying a one-dimensional DWT column-wise on the subbands (intermediate result), four subbands LL, LH, HL, and HH are obtained with the size of $\frac{M}{2}$ x $\frac{N}{2}$, respectively. LH, HL and HH contain the high-frequency information around discontinuities (edges in an image) in the input signal. LL is a coarser version of the original input signal and provides an input to the next decomposition level. The reconstruction is performed oppositely: first on columns, then on rows. Thus, separable 2D DWT has three wavelet functions (m and n are coordinates of the input image):

$$\psi^1(m, n) = \phi(m)\psi(n) \quad LHwavelet \tag{7}$$

$$\psi^2(m, n) = \psi(m)\phi(n) \quad HLwavelet \tag{8}$$

$$\psi^3(m, n) = \psi(m)\psi(n) \quad HHwavelet \tag{9}$$

and one scale function:

$$\phi^2(m, n) = \phi(m)\phi(n) \quad ApproximationLL \tag{10}$$

Figure 1 shows a block diagram of a 2D DWT. An K level decomposition can be performed, resulting in $3K + 1$ different frequency bands: LL is low frequency or approximation coefficients, and the wavelet image coefficients LH, HL, and HH which correspond, respectively, to vertical high frequencies (horizontal edges), horizontal high frequencies (vertical edges), and high frequencies in both directions (corners).

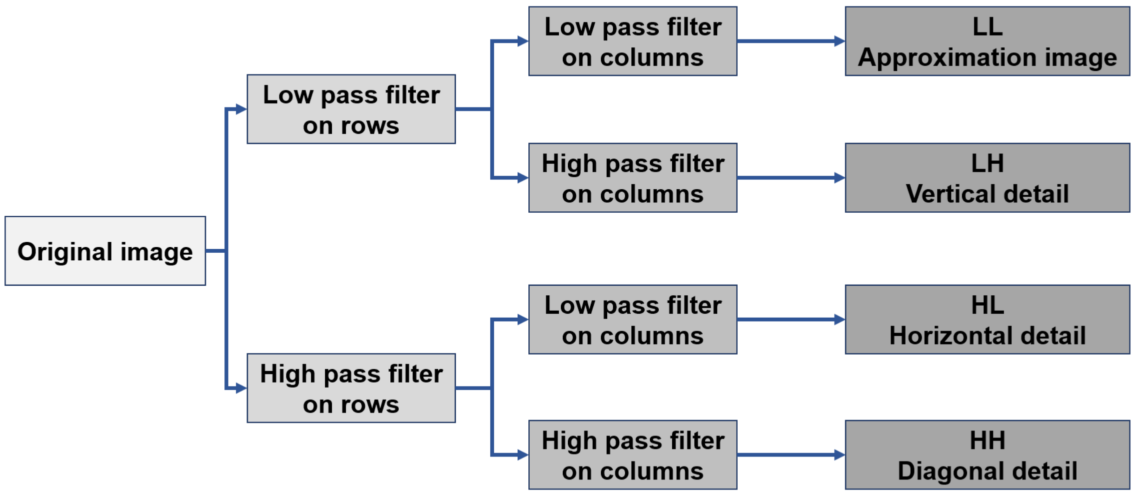

FIG. 1: Block diagram of DWT.

Neural network training strategy

In this project, we propose to use U-Net (Ronneberger et al., 2015) with additional skip connection layers to learn patterns from migrated images and discrete wavelet transform filtered images. The basic U-Net architecture is derived from our previous work (Huang and Trad, 2021). We add another channel, the LL subband, different from the previous inputs, into the neural network input. Figure 2 illustrates the DWT applied U-Net architecture. For the encoder part, we now have three input channels: smooth background reflectivity, RTM images with multiple energy and corresponding LL subband images. Then, the network down-sampling the original images into small sizes to learn key features from residuals and patterns in the data. After that, subsurface structure key features are up-sampled to the original dimensions by transpose convolutions. Additional skip connections work as identity mapping (He et al., 2016), and help to strengthen the training result with weak constraints.

The network operator acts as an approximation of the inverse of the Hessian (Kaur et al., 2020; Torres and Sacchi, 2022) to filter migrated data into a predicted reflectivity model, but with more physical data constraints in the input channel. The solution can be determined as:

$$\mathbf{m}_{pred} = \mathbf{\Gamma}_{unet}(\mathbf{m}_{rtmm}, \mathbf{m}_{smooth\_refl}, \mathbf{m}_{rtmm_{DWT}},), \tag{11}$$

where $\mathbf{m}_{rtmm}$ is the RTMM initial image, $\mathbf{m}_{smooth\_refl}$ denotes the smooth background reflectivity model, $\mathbf{m}_{rtmm_{DWT}}$ means DWT subband on RTMM image, and $\mathbf{m}_{pred}$ represents the output reflectivity coefficient prediction.

Four neural networks are planned in the workflow: models R1, R2, R3 and R4. Figure 3 illustrates the relation between different models and workflows. Models R2 and R4 are

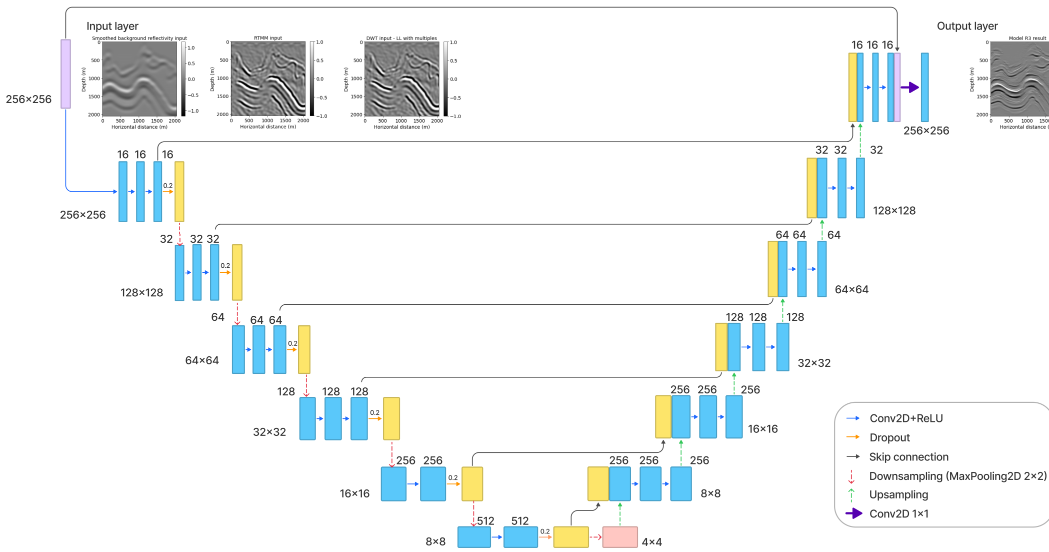

FIG. 2: Architecture of DWT applied in the RTMM-CNN. The main structure is a U-Net with more skip connection layers. The input layer includes three channels: background reflectivity, RTMM image, and subband LL after using DWT of RTMM image. Predicted reflection coefficient is the output.

treated as pre-trained models using true reflectivity and its RTMM image, and DWT subband as the input. The pre-conditioned models R2 and R4 can minimize the appropriate parameters range for the next steps of fine-tuning training. Then, models R1 and R3 are fine-tuned based on R2 and R4's parameters, respectively. Since we are concerned about the results influenced by the DWT subband and multiple energy, in the next section, we will mainly make a comparison between results from models R1, R3 and R4.

Measurements

Mean squared error (MSE)

The mean squared error (MSE) loss is applied to evaluate the model performance and penalize the large prediction errors:

$$\mathrm{MSE} = \frac{1}{n}\sum_{i=1}^{n}(\mathbf{m}_{pred}^{i} - \mathbf{m}_{true}^{i})^2, \tag{12}$$

where n is the total number of samples, $\mathbf{m}_{pred}$ is derived from equation 12 U-Net using RTMM initial images, and $\mathbf{m}_{true}$ denotes the true reflectivity models.

Peak signal-to-noise ratio (PSNR)

A peak signal-to-noise ratio (PSNR) is used to evaluate the model performance:

$$\mathrm{PSNR} = 20 * \log_{10}(\frac{\mathrm{MAX}_I}{\sqrt{\mathrm{MSE}}}), \tag{13}$$

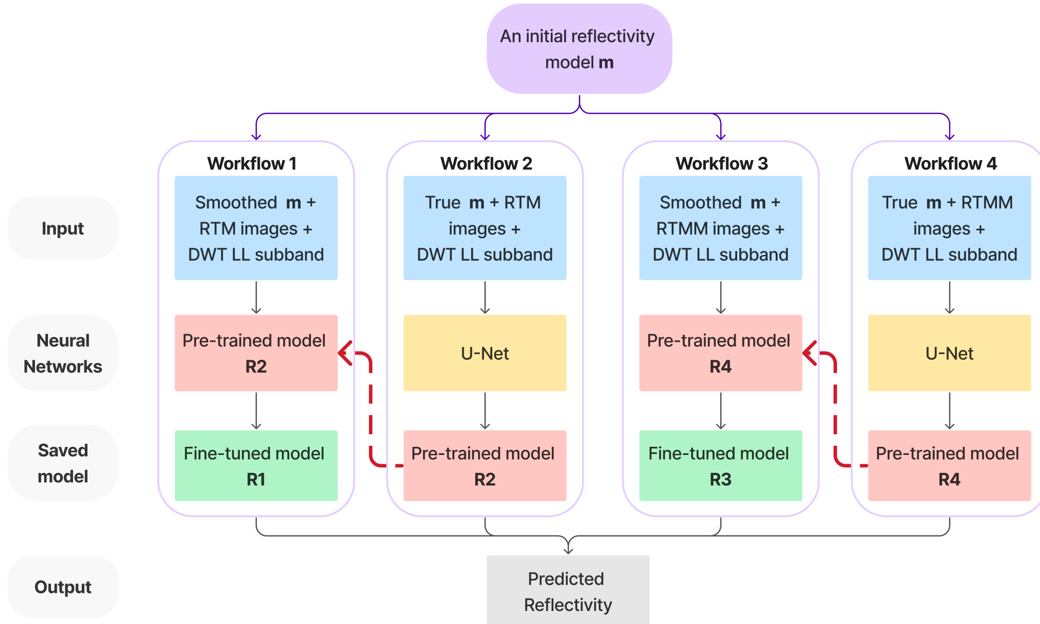

FIG. 3: Neural network model plan and workflows.

where MAX_I denotes the maximum possible pixel value of the image, and MSE is the mean squared error based on the equation 12.

NUMERICAL EXAMPLES

In this section, some numerical examples will be shown to illustrate the approach and show refined predictions on reflectivity with this proposed method.

Train and test set

We've used Sigsbee2b, Amoco, Agbami, Pluto, BP2004 and Marmousi and our defined model as the original input set. Eight meters is used as the spatial interval for each grid point. The total record time is 7.2 seconds with 0.8 of milliseconds temporal sampling. The shot and receiver intervals are 80 and 16 meters, respectively. A fourth-order finite different method is used for the forward modeling. Model R1 in Figure 3 without multiple energy is chosen as our baseline model. Before training, the whole RTM and RTMM images, and the corresponding DWT subband were partly chosen and divided randomly into 1900 different spatial windows with 256x256 points. We did not choose a more significant number of windows because of computation efficiency. The train and test set ratio is 0.8: 0.2. Note that we have not used all the pixels in the migration images, and the new windowing images will be treated as the validation set. All the output predictions have normalized scaling.

Add DWT in NN input as the third channel (LL)

The approximation image LL is considered to contribute to our neural network as the third channel input (the first channel is the initial migration image, and the second channel is smoothed background reflectivity), because it inherits major patterns from the initial migration images and also contains some low-frequency information due to the low pass filter. For example, Figure 4 shows different subbands after discrete wavelet transform on the Pluto geology model. Subbands LL and LH can maintain much information on geologic structures compared with HL and HH. Furthermore, low-frequency subband can help to avoid neural networks having a strong dependency on other input channels, for example, the background, reflectivity.

The proposed technique has been tested on the Foothills and Overthrust geology models respectively. When windowing the inputs, to obtain a subband LL image with the same size as input migration images, we applied a bicubic interpolation with factor 2 on the LL image.

Foothills

Figure 5 gives predictions on Foothills by models R1, R3 and R4, respectively. Model R3 (5f) result, which contains multiple energy, has improved resolution and accurate reflector prediction than R1 (5e) or R4 (5g). Model R4 gives model R3 optimized preconditioned parameters for R3 to fine-tune. Details of the results are shown in Figure 6 and 7. Two of three input channels are listed on the first row, including smooth background reflectivity, RTM image and RTMM image. The second row in both figures from left to right contains the true label, DWT input subband LL, and LL with multiples. So, LL without multiples is the input of model R1, and LL with multiples is fed into R3. As subband LL is extracted from initial migration images, it stays most key features of geologic events with lower frequency. In this project, we smooth the background reflectivity with Gaussian smoother. The predictions in both examples (Figure 6 and 7g) provides a pre-conditioning effect and cannot give refined resolution. On the other hand, model R3, which contains DWT subband LL input, can generate enhanced predictions (Figure 6 and 7i) and suppress artifacts properly. Precisely, lateral velocity variation and fault details are recovered properly in model R3 prediction. Additionally, compared with model R1 predictions, which also use an LL input channel, R3 gives better resolution and illumination on structures and faults because of having useful multiple energy. The PSNR values in table 1 also prove R3 has the highest value and performance than other neural network models.

Overthrust

For the Overthrust example, Figure 8-10 indicate total and windowed predicted results by models R1, R3 and R4. Similar to the previous example result, after combining the DWT subband LL, model R3 with multiples can predict reflectivity with high resolution and accuracy. For example, the thin layer structure in Figure 10 can be predicted with better accuracy by model R3 (Figure 10f), where the amplitude near the fault on the top has clear differences to indicate.

Please note that, in Figure 9, the model R1 PSNR value for Overthrust example 1 is a

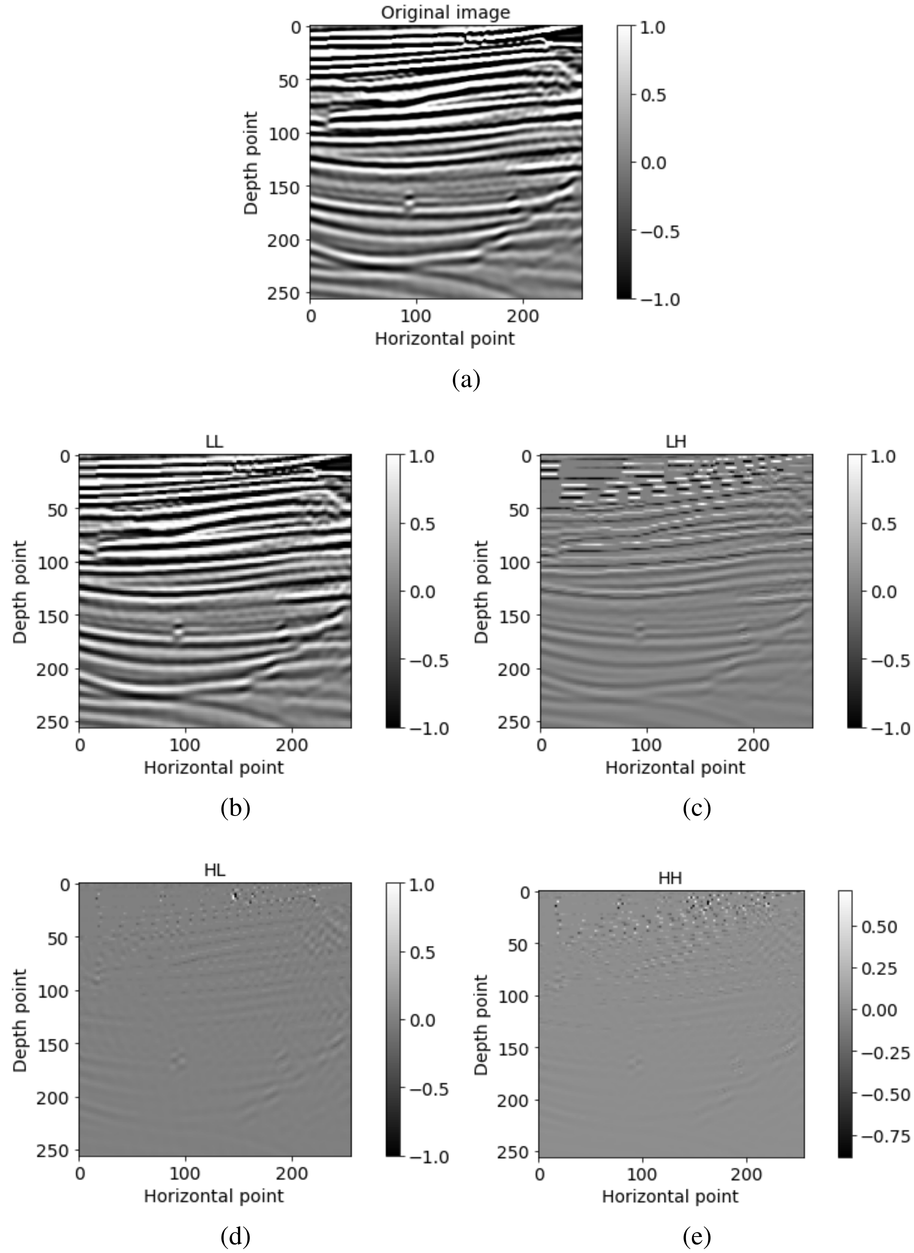

FIG. 4: Original image (a) was decomposed by Haar discrete wavelet transform and result (b) LL (c) LH (d) HL (e) HH were obtained by filter banks with interpolation.

bit larger than that of model R3, even though the R3 result gives a more accurate prediction on thrust structure. The possible reason could be that predictions by model R3 still have some artifacts that are larger than model R1 prediction, although model R3 can give a better image resolution.

Add DWT and var=0.02 noise in the NN input

To make the synthetic data more realistic and test the neural network generalization ability, we add Gaussian noise on the migration images (RTM/RTMM) with a variance equal to 0.02. Please note that neural network models are new to Gaussian noise data, which means we have not trained models with Gaussian noise added before.

Figures 11-13 give the comparison of Foothills example, and figures 14-16 show the Overthrust example observation. After adding Gaussian noise, reflection events are even hardly distinguished from noise in both examples. Precisely, in Figure 16, horizontal events at deep depth are blurred and covered by noise. Since migration with multiples can provide useful information about reflection events, RTMM input (For example, Figure 16c) has higher signal amplitude. Even though the LL subband provides low-frequency information, the model R3 prediction can still extract main events from migrated images with high resolution. Similarly, for the rest of the windowed examples, the predictions by model R3 of Foothills and Overthrust are consistent with the noise-free results, which have more clear predictions with boosted resolution and accuracy compared with the model R1 predictions.

DISCUSSION

Previously, we mentioned that this project's neural network architecture is based on our previous work (Huang and Trad, 2021). At that time, we trained our models with a small smooth parameter (filter's half width is 5-point). In this project, except for the 5-point smoother, we amended the fine-tuned model with a larger smooth parameter - 9 points. In this section, we will compare our previous models with models in this project with the same 5-point smoother parameter used.

Figures 17-18 are the comparison of Foothills and Overthrust sampled windows. Original RTMM-CNN denotes our previous model, and RTMM-CNN with DWT subband means the model in this project. Please note that the models we compare here are model R3, using smooth background reflectivity and RTMM images as inputs. In this comparison, both models are not fine-tuned with a 9-point half-width smoother.

RTMM-CNN with DWT subband has a better prediction on the Overthrust example shown in Figure 18. For example, thin layer events can be recovered with high resolution in Figure 18b. Noise can be suppressed properly in Figure 18d compared with c, which the original RTMM-CNN generates. On the other hand, the original RTMM-CNN can handle the Foothills example with enhanced image quality than the model using the DWT channel. Tables 5 and 6 show that the PSNR of the original RTMM-CNN is larger in the Foothills example, but smaller in the Overthrust example, compared with RTMM-CNN with DWT subband. Thus, original RTMM-CNN can work with rapid lateral velocity variation geology models; on the other hand, RTMM-CNN with DWT subband is capable of thin-layered structures.

CONCLUSIONS

RTMM-CNN with a DWT subband channel can provide improved reflectivity coefficient prediction. DWT subband LL and pre-trained model let the fine-tuned model learn to extract key features from low-frequency information and tolerate more artifacts from smooth input. Multiple energy is a supplement tool providing additional subsurface illumination, and helping neural network distinguish signals from noise. The neural network operator acts as an approximation of the inverse of the Hessian, which can suppress image artifacts and improve the reflectivity resolution. The next step is to let the model learn how to predict a geology model with rapid lateral velocity change and test it in the field data.

ACKNOWLEDGEMENTS

We thank the sponsors of CREWES for continued support. This work was funded by CREWES industrial sponsors and NSERC (Natural Science and Engineering Research Council of Canada) through the grant CRDPJ 543578-19. The first author was partially supported by a scholarship from the China Scholarship Council (CSC).

REFERENCES

Acharya, T., and Ray, A. K., 2005, Image processing: principles and applications, Chapter 5: John Wiley & Sons.

Baysal, E., Kosloff, D. D., and Sherwood, J. W., 1983, Reverse time migration: Geophysics, **48**, No. 11, 1514–1524.

Dong, S., Cai, J., Guo, M., Suh, S., Zhang, Z., Wang, B., and Li, e. Z., 2012, Least-squares reverse time migration: Towards true amplitude imaging and improving the resolution, *in* SEG technical program expanded abstracts 2012, Society of Exploration Geophysicists, 1–5.

Ghazali, K. H., Mansor, M. F., Mustafa, M. M., and Hussain, A., 2007, Feature extraction technique using discrete wavelet transform for image classification, *in* 2007 5th Student Conference on Research and Development, IEEE, 1–4.

Gray, S. H., Etgen, J., Dellinger, J., and Whitmore, D., 2001, Seismic migration problems and solutions: Geophysics, **66**, No. 5, 1622–1640.

He, K., Zhang, X., Ren, S., and Sun, J., 2016, Identity mappings in deep residual networks, *in* European conference on computer vision, Springer, 630–645.

Huang, S., and Trad, D., 2021, Convolutional neural network-based reverse time migration with multiple energy: CREWES Research Report, **33**, 18.

Kaur, H., Pham, N., and Fomel, S., 2020, Improving the resolution of migrated images by approximating the inverse hessian using deep learning: Geophysics, **85**, No. 4, WA173–WA183.

Levin, S. A., 1984, Principle of reverse-time migration: Geophysics, **49**, No. 5, 581–583.

Li, Z., Li, Z., Wang, P., and Zhang, M., 2017, Reverse time migration of multiples based on different-order multiple separation: Geophysics, **82**, No. 1, S19–S29.

Liu, N., Wu, L., Wang, J., Wu, H., Gao, J., and Wang, D., 2022, Seismic data reconstruction via wavelet-based residual deep learning: IEEE Transactions on Geoscience and Remote Sensing, **60**, 1–13.

Liu, Y., Chang, X., Jin, D., He, R., Sun, H., and Zheng, Y., 2011, Reverse time migration of multiples for subsalt imaging: Geophysics, **76**, No. 5, WB209–WB216.

McMechan, G. A., 1983, Migration by extrapolation of time-dependent boundary values: Geophysical prospecting, **31**, No. 3, 413–420.

Ronneberger, O., Fischer, P., and Brox, T., 2015, U-net: Convolutional networks for biomedical image segmentation, *in* International Conference on Medical image computing and computer-assisted intervention, Springer, 234–241.

Schuster, G. T., 2020, Seismic imaging, overview: Springer International Publishing.

Suraj, A. A., Francis, M., Kavya, T., and Nirmal, T., 2014, Discrete wavelet transform based image fusion and de-noising in fpga: Journal of Electrical Systems and Information Technology, **1**, No. 1, 72–81.

Torres, K., and Sacchi, M., 2021, Deep learning based least-squares reverse-time migration, *in* First International Meeting for Applied Geoscience & Energy, Society of Exploration Geophysicists, 2709–2713.

Torres, K., and Sacchi, M., 2022, Least-squares reverse time migration via deep learning-based updating operators: Geophysics, **87**, No. 6, 1–80.

Vamaraju, J., Vila, J., Araya-Polo, M., Datta, D., Sidahmed, M., and Sen, M. K., 2021, Minibatch least-squares reverse time migration in a deep-learning framework: Geophysics, **86**, No. 2, S125–S142.

Wang, X.-Y., Yang, H.-Y., and Fu, Z.-K., 2010, A new wavelet-based image denoising using undecimated discrete wavelet transform and least squares support vector machine: Expert Systems with Applications, **37**, No. 10, 7040–7049.

Wang, Y., Zheng, Y., Xue, Q., Chang, X., Fei, T. W., and Luo, Y., 2017, Reverse time migration of multiples: Reducing migration artifacts using the wavefield decomposition imaging condition: Geophysics, **82**, No. 4, S307–S314.

Whitmore, N. D., 1983, Iterative depth migration by backward time propagation, *in* SEG Technical Program Expanded Abstracts 1983, Society of Exploration Geophysicists, 382–385.

Wu, D., Li, Q., Zhang, X., Li, J., and Wu, H., 2018, Least-squares reverse time migration with adaptive moment estimation method, *in* 2018 SEG International Exposition and Annual Meeting, OnePetro.

Wu, H.-C., Fan, W.-L., Tsai, C.-S., and Ying, J. J.-C., 2022, An image authentication and recovery system based on discrete wavelet transform and convolutional neural networks: Multimedia Tools and Applications, **81**, No. 14, 19,351–19,375.

Zhang, W., Gao, J., Cheng, Y., Li, Z., Jiang, X., and Zhu, J., 2022, Deep-learning for accelerating prestack correlative least-squares reverse time migration: Journal of Applied Geophysics, **200**, 104,645.

Zhang, Y., Liu, Y., Liu, X., and Zhou, X., 2020, Reverse time migration using water-bottom-related multiples: Geophysical Prospecting, **68**, No. 2, 446–465.

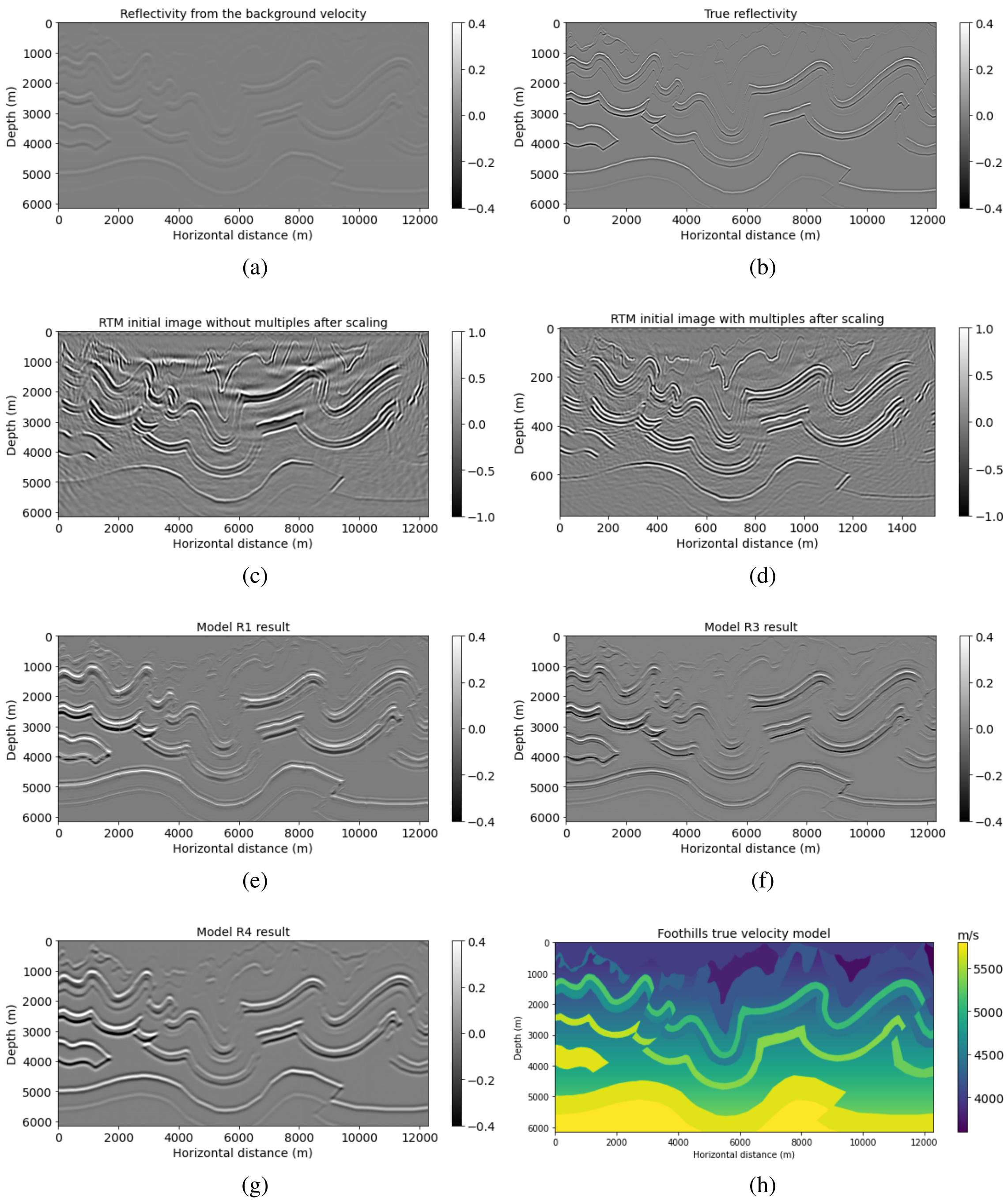

FIG. 5: Foothills model results. (a) Reflectivity from the background velocity, (b) true band-limited reflectivity, (c) RTM image without multiple energy, (d) RTM image with multiple energy, (e) model R1 result based on workflow 1, (f) model R3 result based on workflow 3, (g) model R4 result based on workflow 4, and (h) true Foothills velocity.

Table 1: PSNR (dB) comparison for Foothills example			
Prediction	Model R1	**Model R3**	Model R4
Total Foothills	21.94	**23.28**	18.08
Example 1	18.03	**19.27**	14.01
Example 2	16.75	**17.18**	13.81

Table 1: PSNR (dB) comparison for Foothills example.

Table 2: PSNR (dB) comparison for Overthrust example			
Prediction	Model R1	**Model R3**	Model R4
Total Overthrust	17.21	**18.83**	15.05
Example 1	**17.90**	16.80	14.03
Example 2	13.18	**13.25**	10.21

Table 2: PSNR (dB) comparison for Overthrust example.

Table 3: PSNR (dB) comparison for Foothills example with var=0.02 noise			
Prediction	Model R1	**Model R3**	Model R4
Total Foothills	21.89	**23.27**	18.08
Example 1	18.01	**19.22**	14.03
Example 2	16.77	**16.88**	13.99

Table 3: PSNR (dB) comparison for Foothills example with noise added.

Table 4: PSNR (dB) comparison for Overthrust example with var=0.02 noise			
Prediction	Model R1	**Model R3**	Model R4
Total Overthrust	17.23	**18.82**	15.09
Example 1	**17.90**	16.82	14.14
Example 2	13.16	**13.20**	10.25

Table 4: PSNR (dB) comparison for Overthrust example with noise added.

Table 5: PSNR (dB) Foothills comparison between two models		
Prediction	**RTMM-CNN model R3**	RTMM-CNN with DWT model R3
Total Foothills	**21.39**	20.51
Example 1	**17.39**	16.43
Example 2	**13.50**	12.67

Table 5: PSNR (dB) Foothills comparison between original RTMM-CNN and RTMM-CNN with DWT, with noise added.

Table 6: PSNR (dB) Overthrust comparison between two models		
Prediction	RTMM-CNN model R3	**RTMM-CNN with DWT model R3**
Total Overthrust	16.47	**17.84**
Example 1	13.21	**13.43**
Example 2	16.34	**17.35**

Table 6: PSNR (dB) Overthrust comparison between original RTMM-CNN and RTMM-CNN with DWT, with noise added.

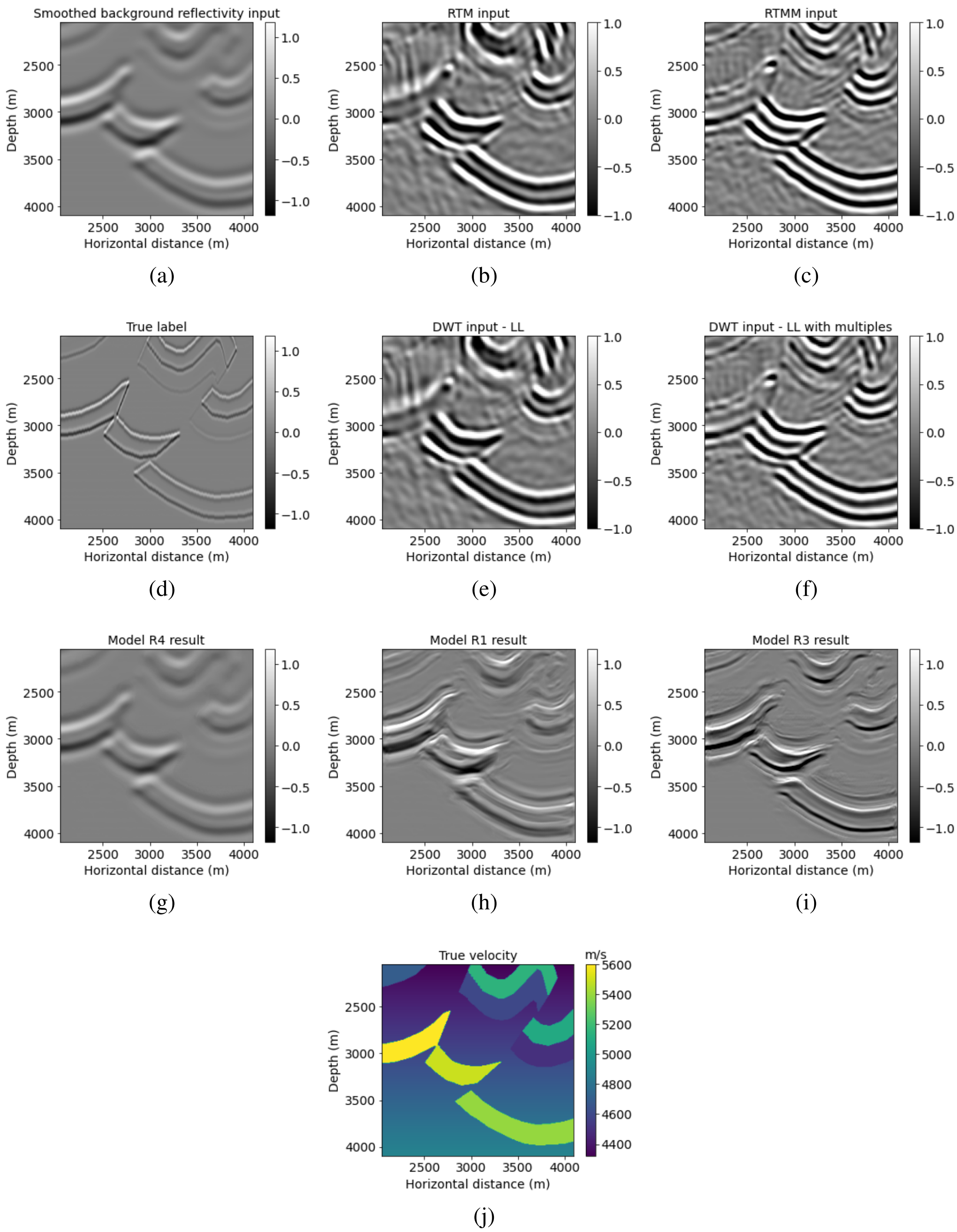

FIG. 6: Foothills example 1 results. (a) Reflectivity from the background velocity, (b) true windowed band-limited reflectivity, (c) RTM image without multiple energy, (d) true label, (e) DWT subband LL without multiple energy, (f) DWT subband LL with multiple energy, (g) model R4 result based on workflow 4, (h) model R1 result based on workflow 1, (i) model R3 result based on workflow 3, and (j) true windowed velocity.

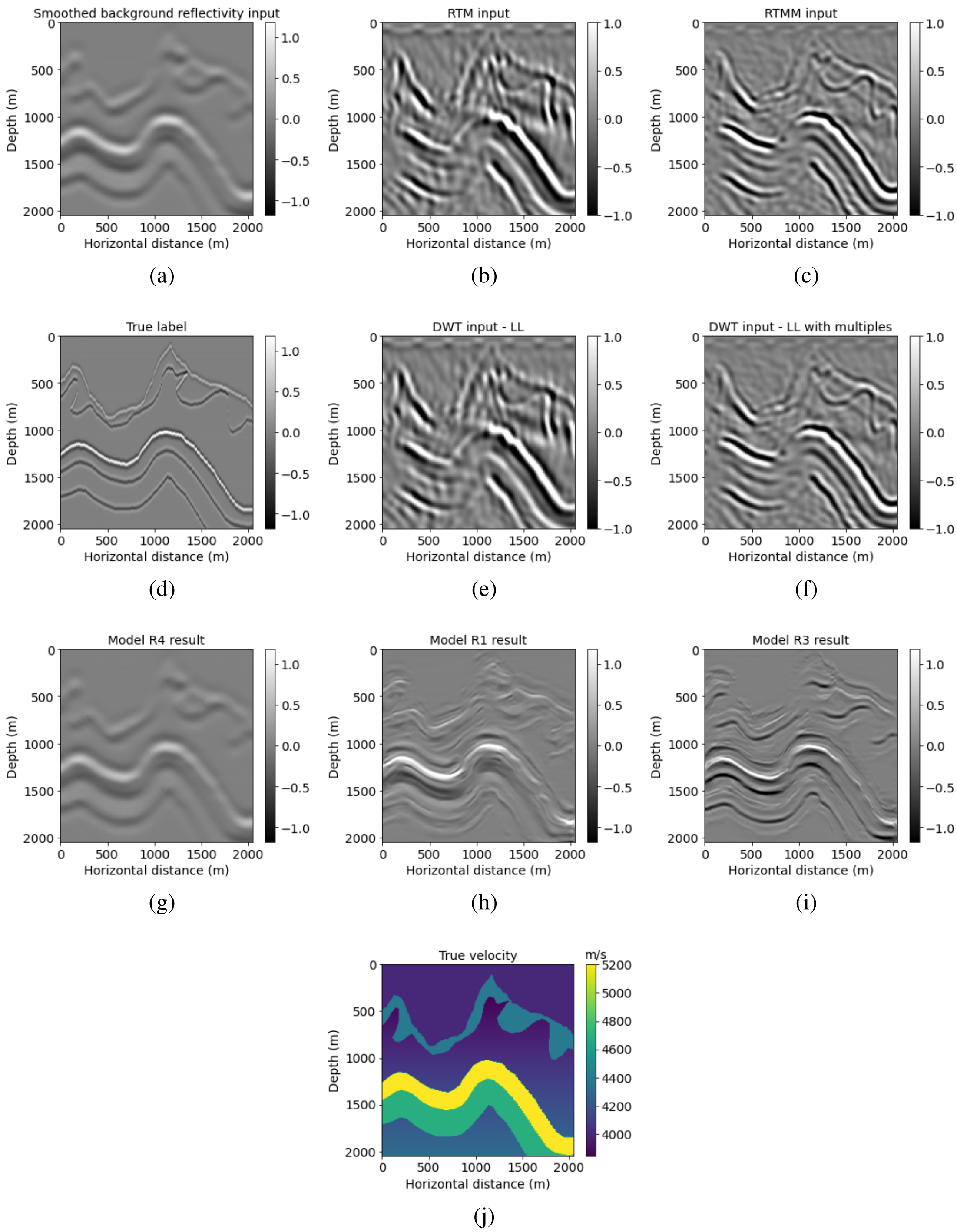

FIG. 7: Foothills example 2 results. (a) Reflectivity from the background velocity, (b) true windowed band-limited reflectivity, (c) RTM image without multiple energy, (d) true label, (e) DWT subband LL without multiple energy, (f) DWT subband LL with multiple energy, (g) model R4 result based on workflow 4, (h) model R1 result based on workflow 1, (i) model R3 result based on workflow 3, and (j) true windowed velocity.

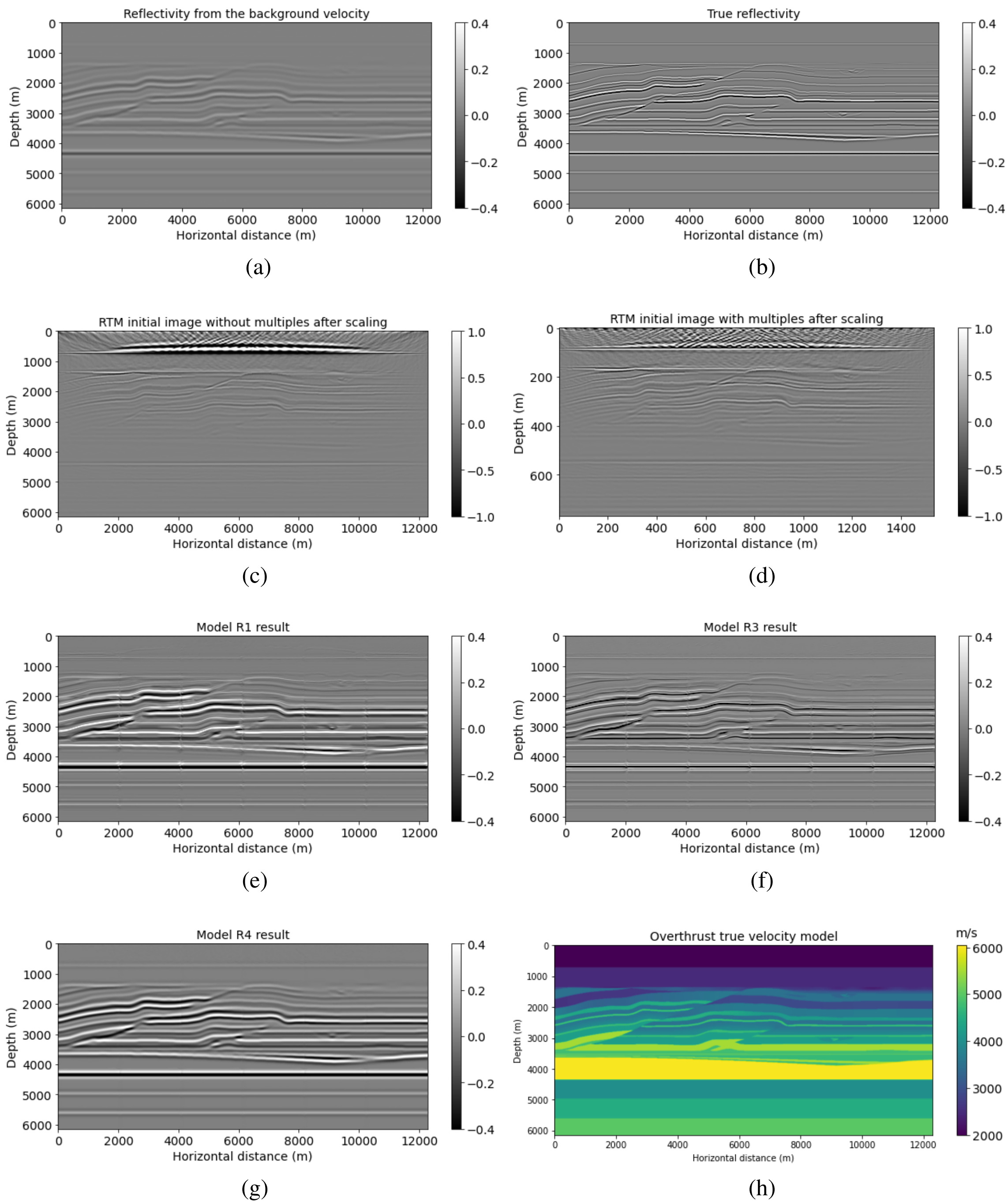

FIG. 8: Overthrust model results. (a) Reflectivity from the background velocity, (b) true band-limited reflectivity, (c) RTM image without multiple energy, (d) RTM image with multiple energy, (e) model R1 result based on workflow 1, (f) model R3 result based on workflow 3, (g) model R4 result based on workflow 4, and (h) true Overthrust velocity.

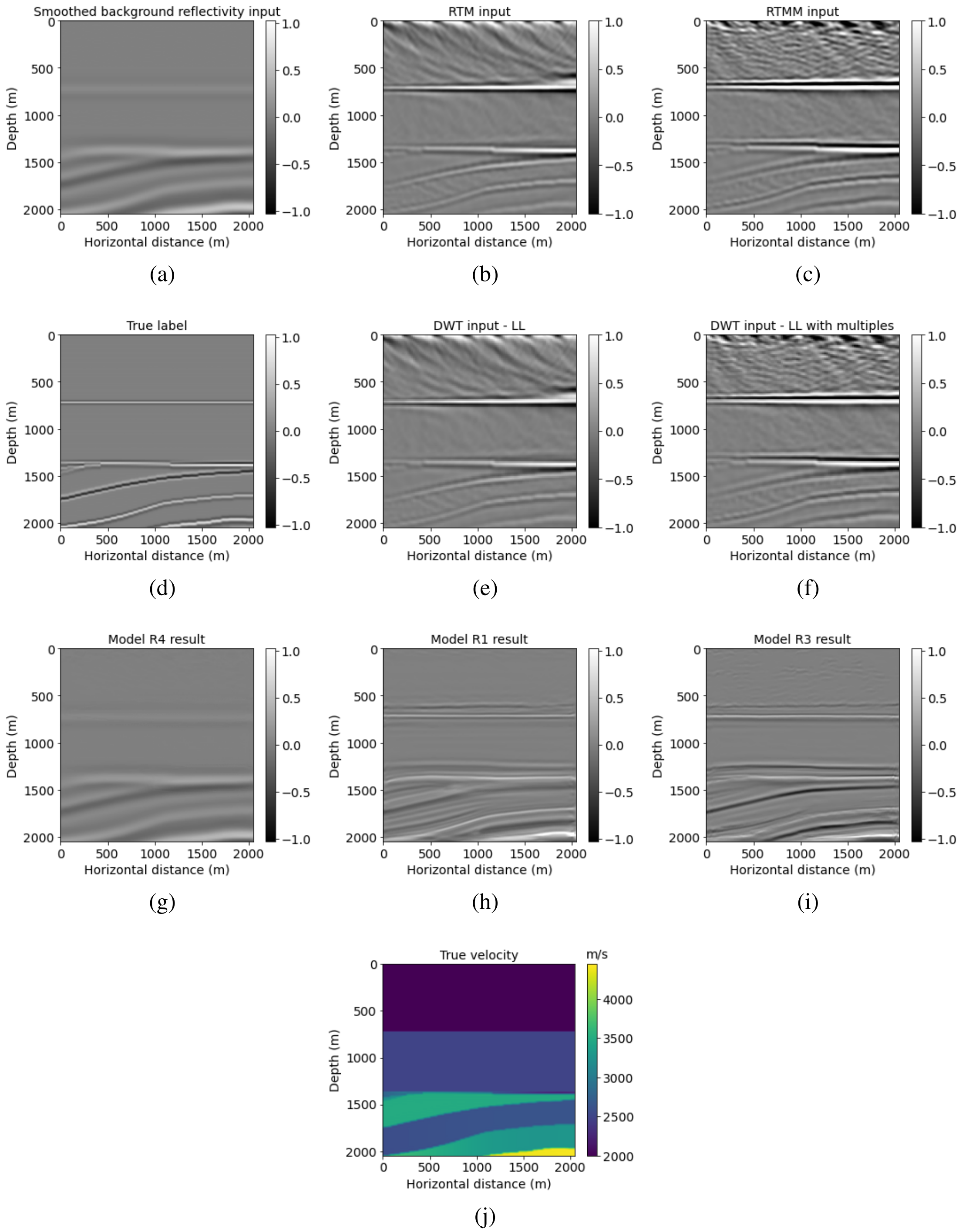

FIG. 9: Overthrust example 1 results. (a) Reflectivity from the background velocity, (b) true windowed band-limited reflectivity, (c) RTM image without multiple energy, (d) true label, (e) DWT subband LL without multiple energy, (f) DWT subband LL with multiple energy, (g) model R4 result based on workflow 4, (h) model R1 result based on workflow 1, (i) model R3 result based on workflow 3, and (j) true windowed velocity.

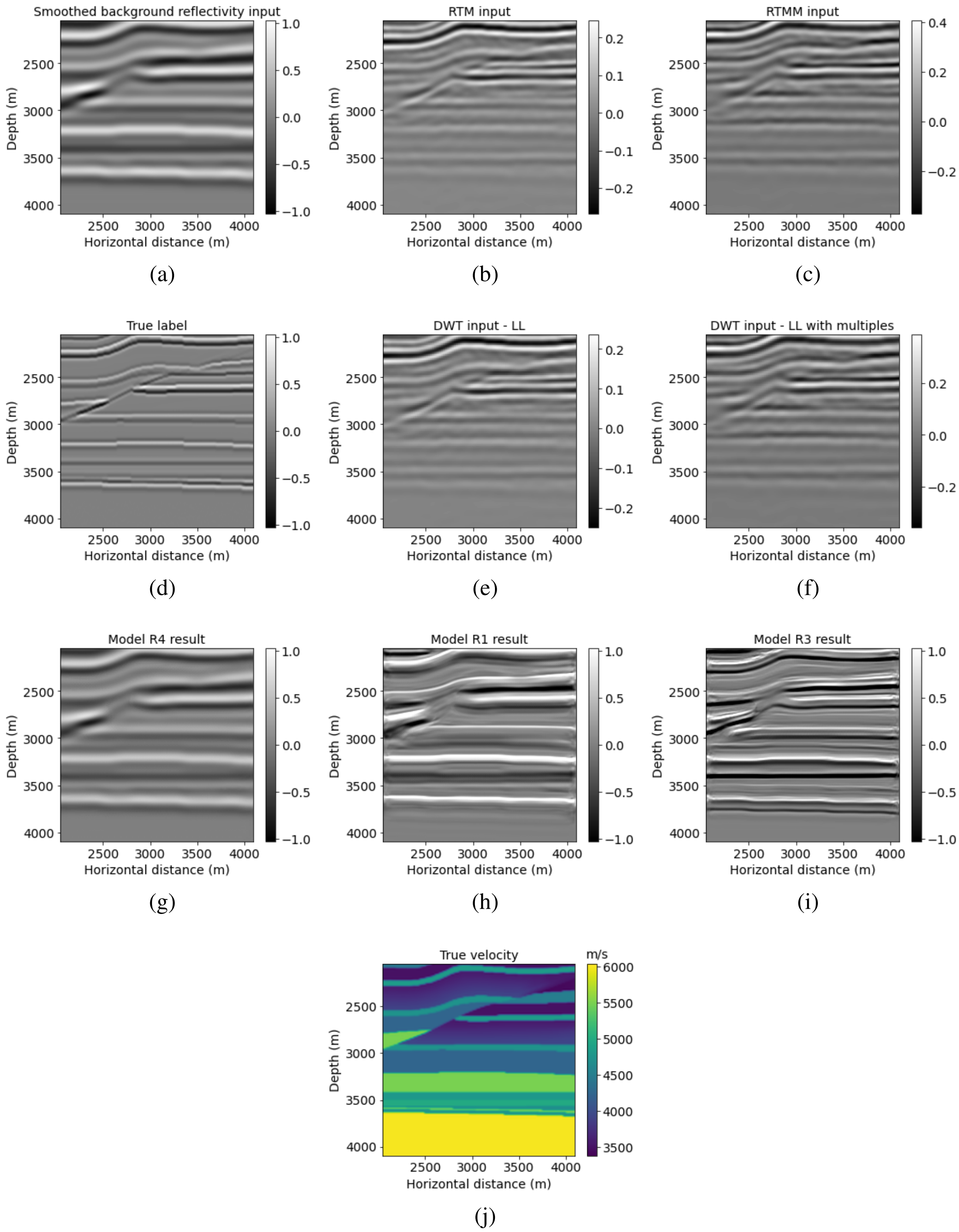

FIG. 10: Overthrust example 2 results. (a) Reflectivity from the background velocity, (b) true windowed band-limited reflectivity, (c) RTM image without multiple energy, (d) true label, (e) DWT subband LL without multiple energy, (f) DWT subband LL with multiple energy, (g) model R4 result based on workflow 4, (h) model R1 result based on workflow 1, (i) model R3 result based on workflow 3, and (j) true windowed velocity.

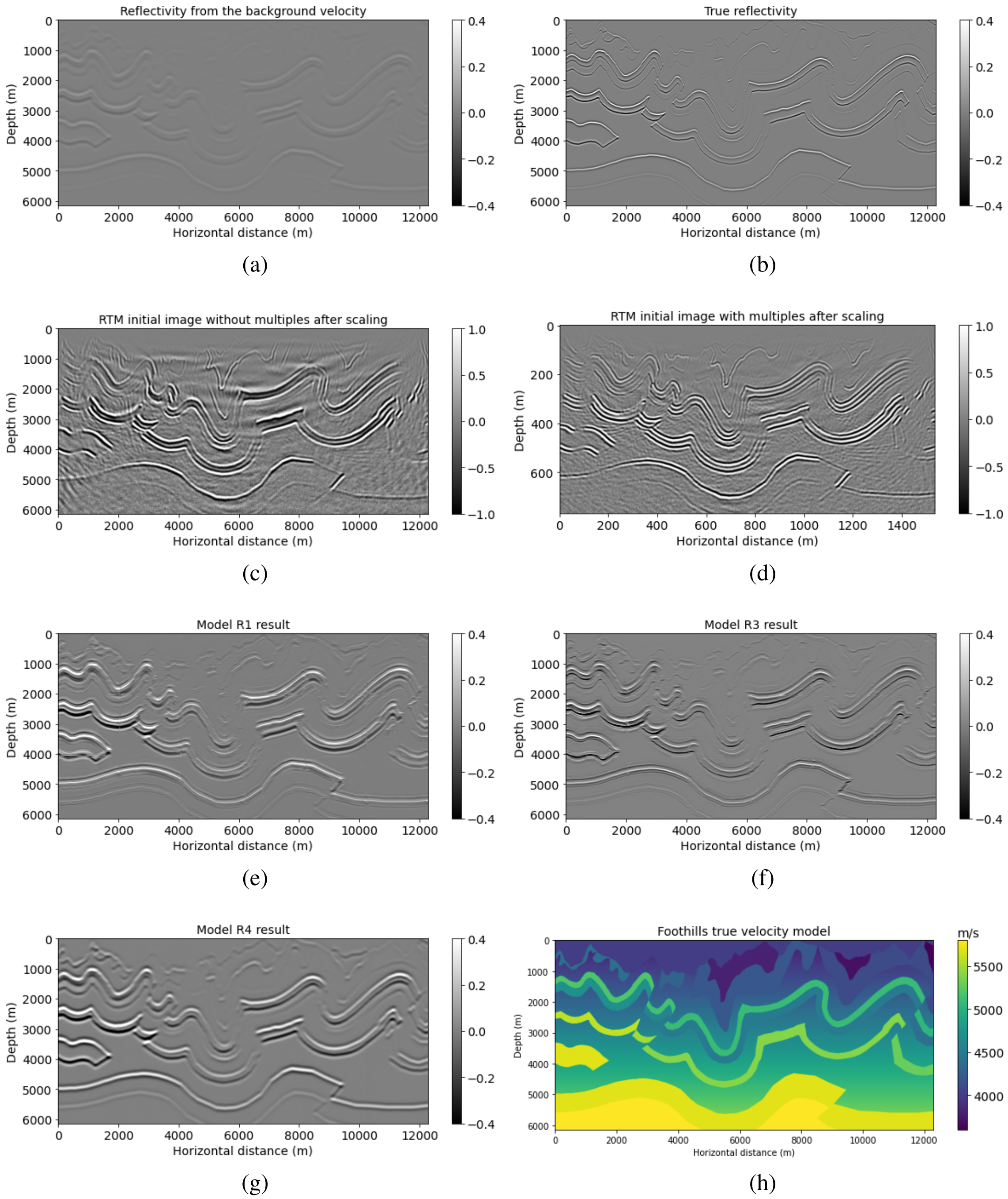

FIG. 11: Foothills model results after adding noise. (a) Reflectivity from the background velocity, (b) true band-limited reflectivity, (c) RTM image without multiple energy, (d) RTM image with multiple energy, (e) model R1 result based on workflow 1, (f) model R3 result based on workflow 3, (g) model R4 result based on workflow 4, and (h) true Foothills velocity.

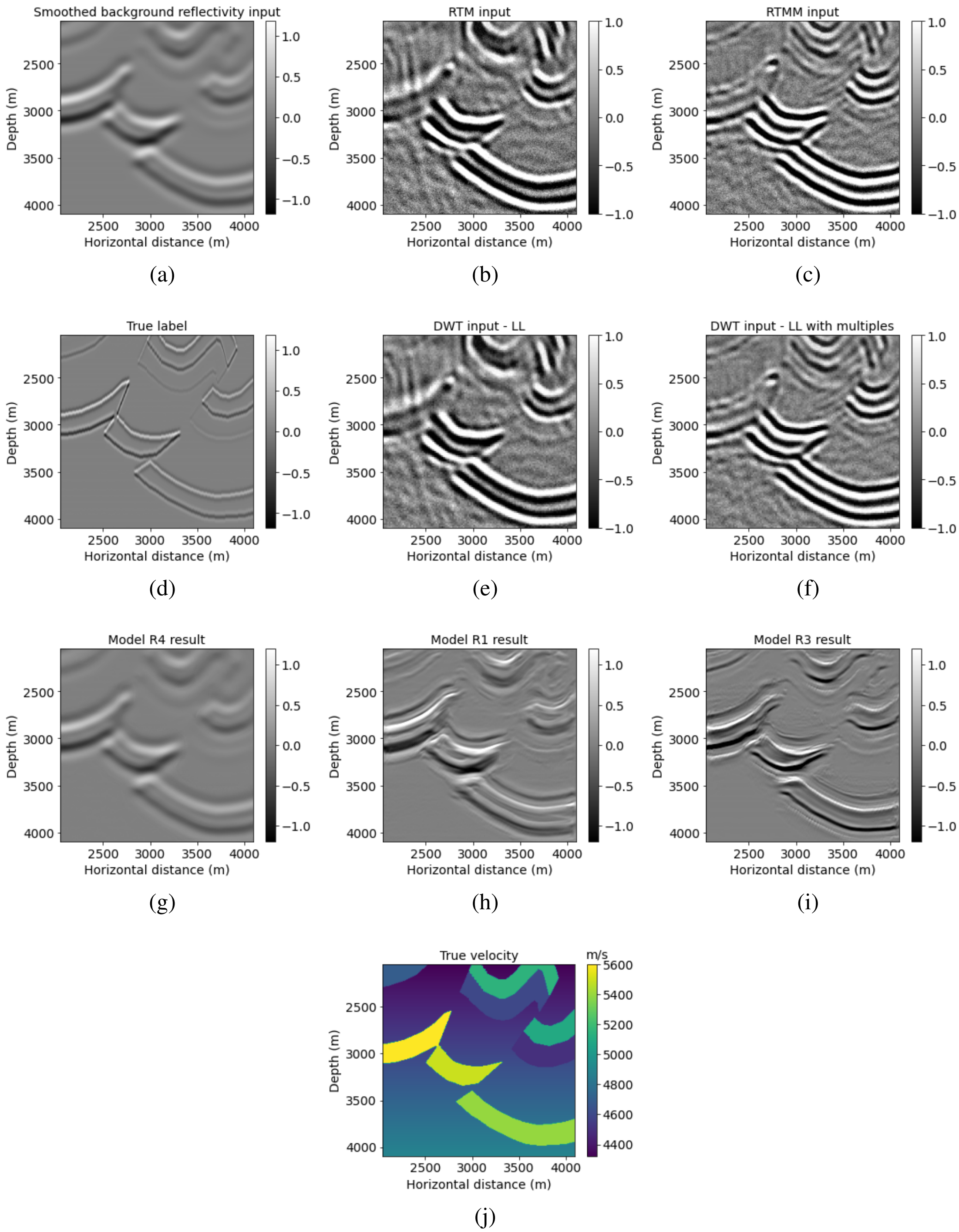

FIG. 12: Foothills example 1 results after adding noise. (a) Reflectivity from the background velocity, (b) true windowed band-limited reflectivity, (c) RTM image without multiple energy, (d) true label, (e) DWT subband LL without multiple energy, (f) DWT subband LL with multiple energy, (g) model R4 result based on workflow 4, (h) model R1 result based on workflow 1, (i) model R3 result based on workflow 3, and (j) true windowed velocity.

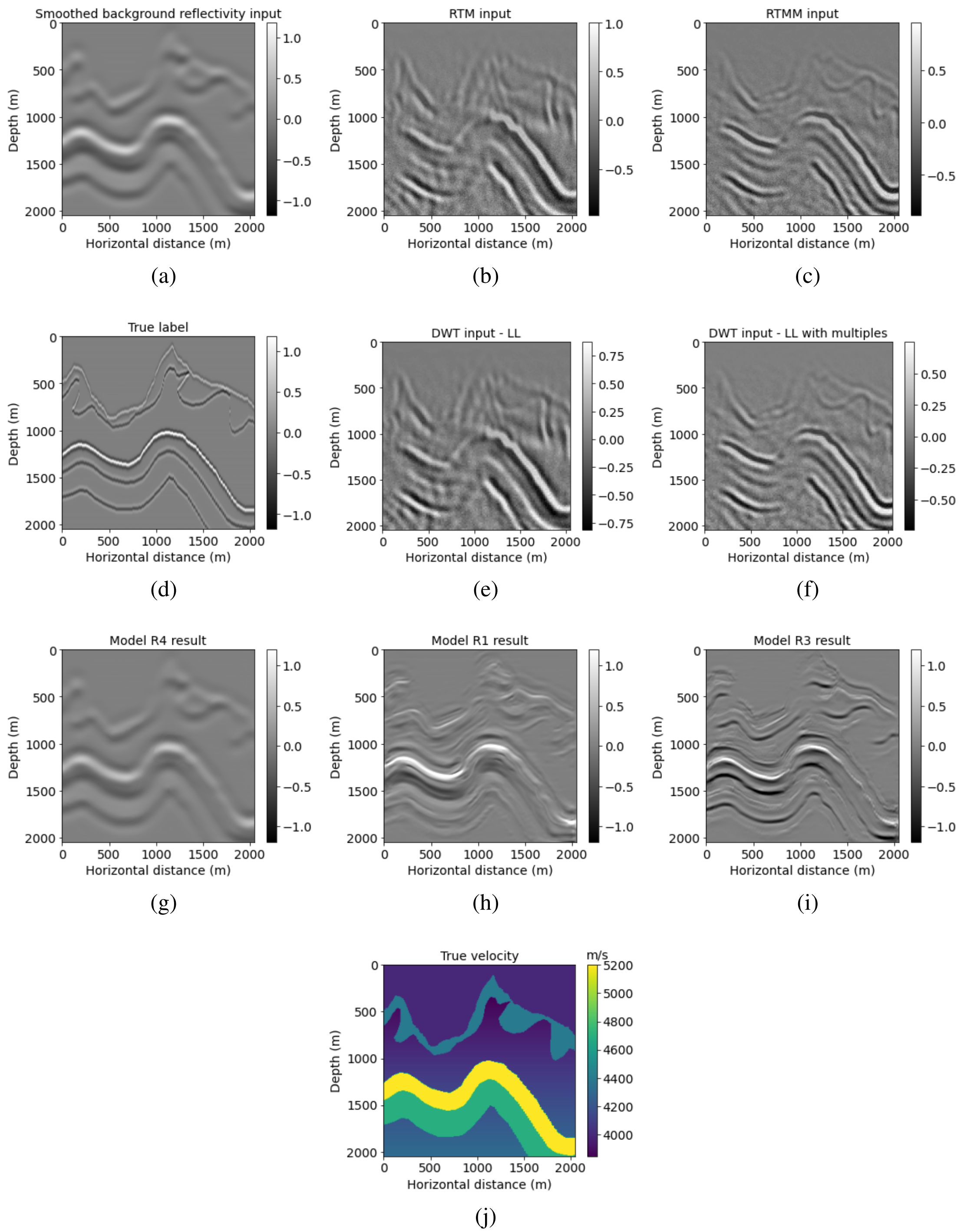

FIG. 13: Foothills example 2 results after adding noise. (a) Reflectivity from the background velocity, (b) true windowed band-limited reflectivity, (c) RTM image without multiple energy, (d) true label, (e) DWT subband LL without multiple energy, (f) DWT subband LL with multiple energy, (g) model R4 result based on workflow 4, (h) model R1 result based on workflow 1, (i) model R3 result based on workflow 3, and (j) true windowed velocity.

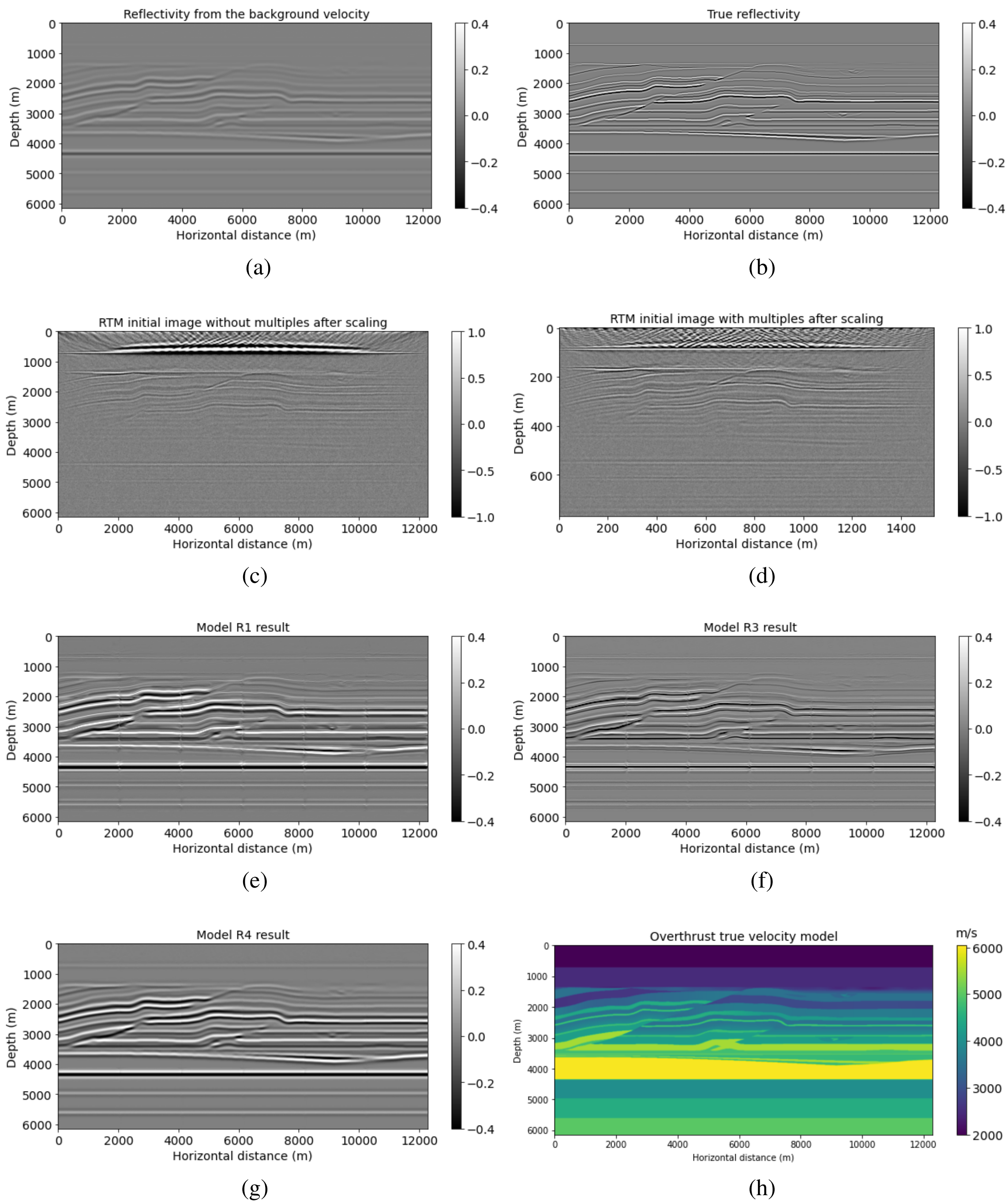

FIG. 14: Overthrust model results after adding noise. (a) Reflectivity from the background velocity, (b) true band-limited reflectivity, (c) RTM image without multiple energy, (d) RTM image with multiple energy, (e) model R1 result based on workflow 1, (f) model R3 result based on workflow 3, (g) model R4 result based on workflow 4, and (h) true Overthrust velocity.

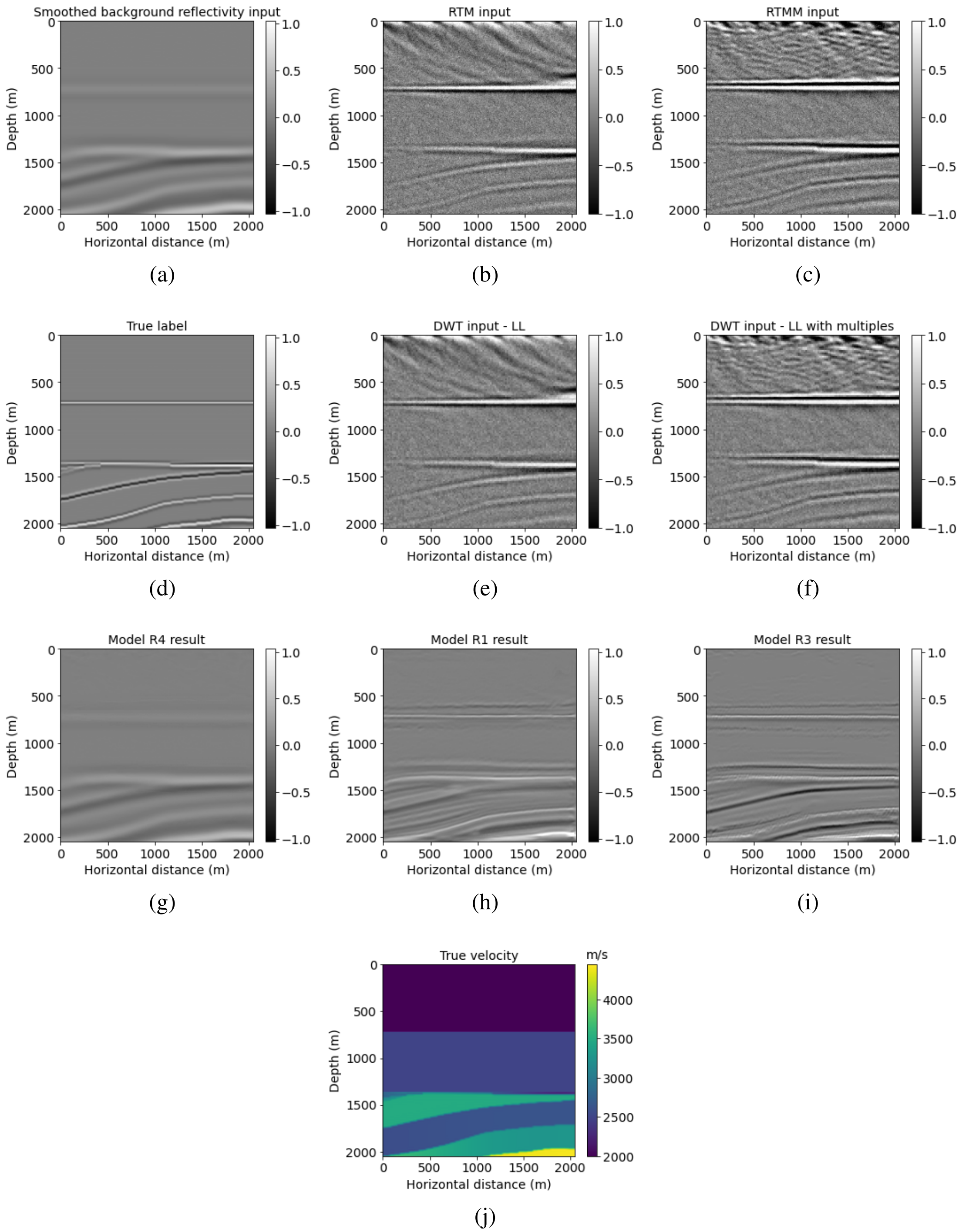

FIG. 15: Overthrust example 1 results after adding noise. (a) Reflectivity from the background velocity, (b) true windowed band-limited reflectivity, (c) RTM image without multiple energy, (d) true label, (e) DWT subband LL without multiple energy, (f) DWT subband LL with multiple energy, (g) model R4 result based on workflow 4, (h) model R1 result based on workflow 1, (i) model R3 result based on workflow 3, and (j) true windowed velocity.

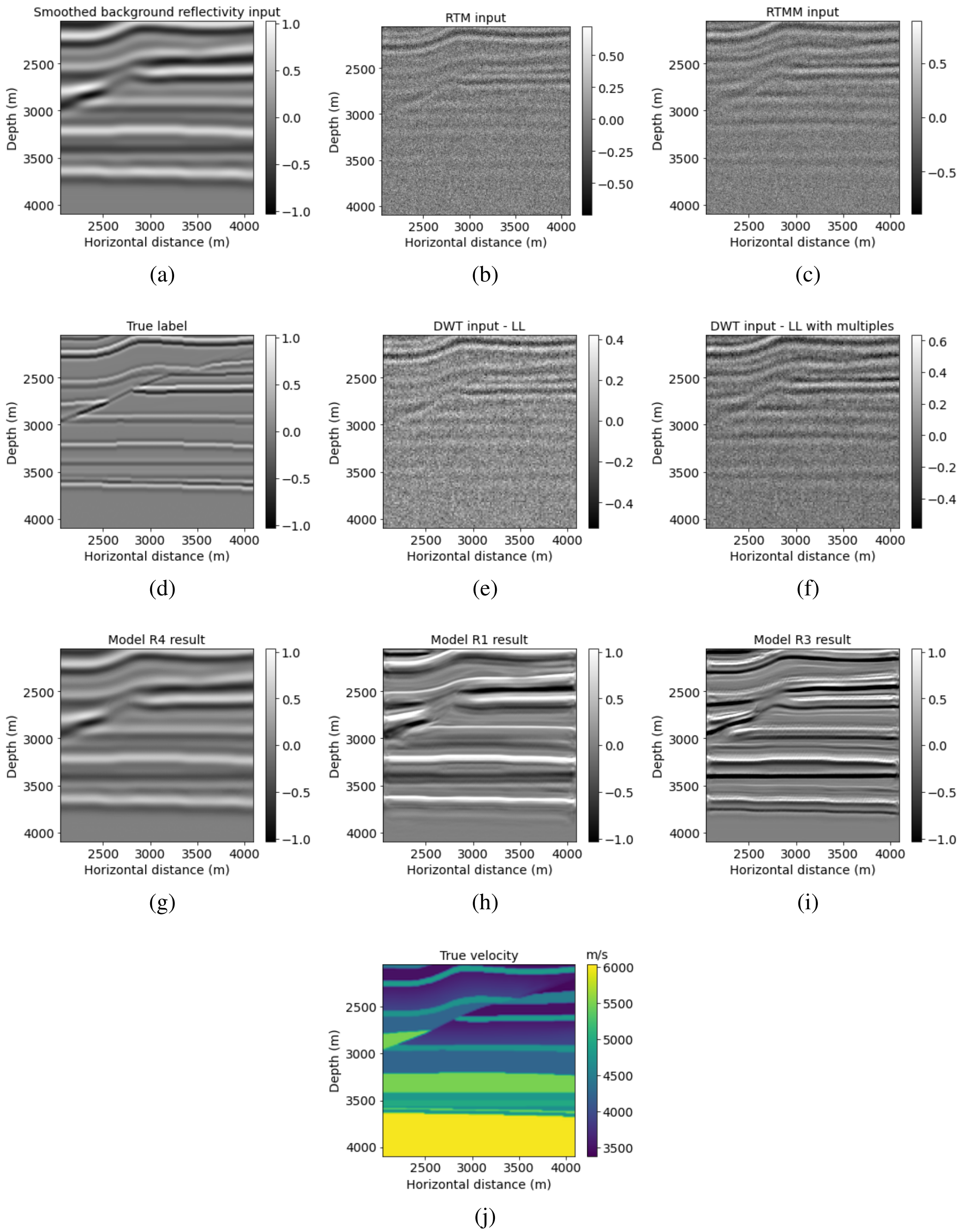

FIG. 16: Overthrust example 2 results after adding noise. (a) Reflectivity from the background velocity, (b) true windowed band-limited reflectivity, (c) RTM image without multiple energy, (d) true label, (e) DWT subband LL without multiple energy, (f) DWT subband LL with multiple energy, (g) model R4 result based on workflow 4, (h) model R1 result based on workflow 1, (i) model R3 result based on workflow 3, and (j) true windowed velocity.

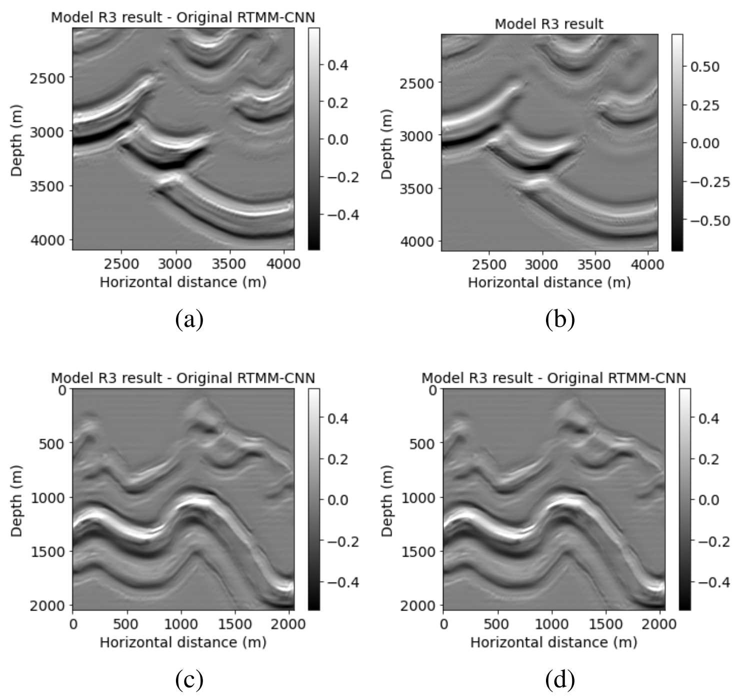

FIG. 17: Foothills example results comparison between original RTMM-CNN and RTMM-CNN with DWT subband. Original RTMM-CNN model R3 predictions on (a) example 1 and (c) example 2. DWT applied RTMM-CNN model R3 predictions on (b) example 1 and (d) example 2.

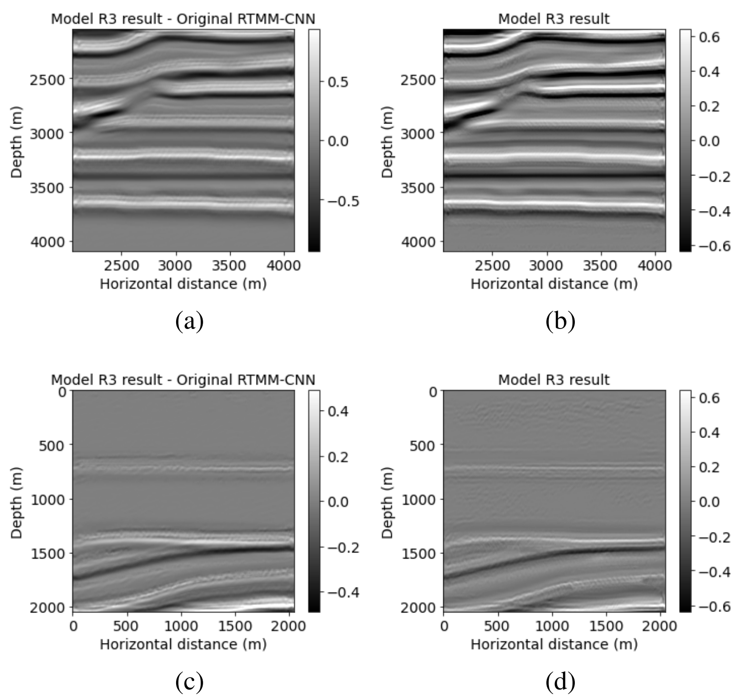

FIG. 18: Overthrust example results comparison between original RTMM-CNN and RTMM-CNN with DWT subband. Original RTMM-CNN model R3 predictions on (a) example 1 and (c) example 2. DWT applied RTMM-CNN model R3 predictions on (b) example 1 and (d) example 2.